The Antares neutrino telescope : performance studies and analysis of first data

Bruijn, R.

Publication date
2008

Chapter 4

Analysis of Line 1 Data

Line 1, the first full detector line of the Antares detector, was deployed on February 14 2006 and connected 16 days later on March 2. Using the algorithm described in chapter 3, the first muon tracks were reconstructed shortly after. This chapter will describe a more detailed analysis of the data that were taken until September 21. On that day the second line was connected, and the analysis of single line data was abandoned in favor of two line data.
In the analysis presented in this chapter, the muon track reconstruction algorithm presented in chapter 3 was used, excluding the full PDF fit.

4.1 Introduction

Line 1 represents a special case for the muon reconstruction. All optical modules are arranged along a single string which can be approximated by a straight line. With this assumption the optical modules are placed at $x = 0, y = 0$. The position is then only defined by z, the position along the line. This introduces a rotational symmetry around the z-axis. The arrival times of Cherenkov photons is no longer dependent on ϕ, and formula 2.5 reduces to a 4-parameter formula [78]. This relation can be derived as follows. A muon traveling with the speed of light emits a Cherenkov photon at position $\vec{e}$, as illustrated in figure 4.1. Position $\vec{o}'$ corresponds to the point where the muon passes the line at the closest distance. The corresponding position on the line is $\vec{o} = (0, 0, z_0)$. The time at which the muon passes point $\vec{o}'$ is defined as t_0. Using the relation $\cos(\theta_c) \times |\vec{a} - \vec{e}| = |\vec{p} - \vec{e}|$, the muon passes position $\vec{a}$ when the photon reaches position $\vec{p} = (0, 0, z)$ where

it is detected at time t. With this it follows :

$$\begin{aligned} c \times (t - t_0) &= |\vec{a} - \vec{o'}| \\ &= -|\vec{o'} - \vec{r}| + |\vec{a} - \vec{r}| \\ &= \cos(\theta) \times (z - z_0) + \frac{|\vec{p} - \vec{r}|}{\tan(\frac{\pi}{2} - \theta_c)} \\ &= \cos(\theta) \times (z - z_0) + \tan(\theta_c)\sqrt{|\vec{r} - \vec{q}|^2 + \vec{p} - \vec{r}|^2} \\ &= \cos(\theta) \times (z - z_0) + \sqrt{n^2 - 1}\sqrt{d^2 + (z - z_0)^2 \sin^2(\theta)} \end{aligned} \tag{4.1}$$

As can be seen in the final expression, the arrival time of the photon is described by a hyperbolic function and is independent of the azimuthal angle ϕ. The asymptotes of the function can be found in the case

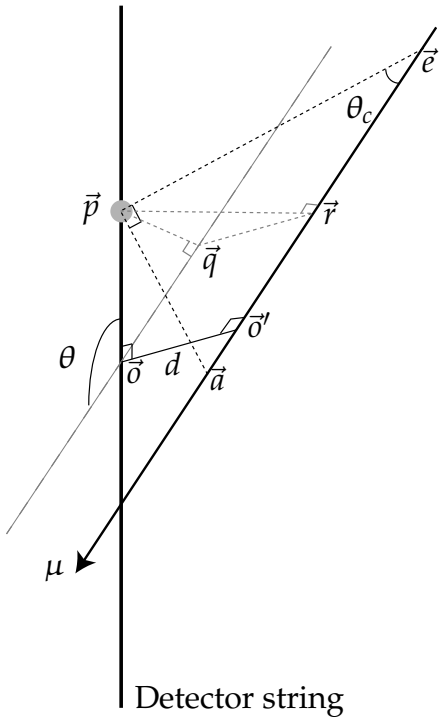

Figure 4.1: *Schematic view of a muon passing a detector line.*

$$|(z - z_0)| \gg \frac{d}{\sin(\theta)} \tag{4.2}$$

By using this assumption

$$c \times (t - t_0) = (z - z_0) \times (\cos(\theta) \pm \sqrt{n^2 - 1}\sin(\theta)) \tag{4.3}$$

and the distance d drops out. So, in this case, the distance d of the muon to the line cannot be determined. Furthermore, equation 4.3 can be simplified to

$$c \times (t - t_0) = (z - z_0) \times n \times \cos(\theta \pm \theta_c) \tag{4.4}$$

From this it can be seen that the two asymptotic solutions differ by $2\theta_c$. Requirement 4.2 can be met when a muon passes above or below the optical modules that record a hit, so that only one side of the Cherenkov cone is seen. In this case it is not possible to distinguish between the two asymptotic solutions and possibly the zenith angle of the muon is reconstructed with an offset of $2\theta_c$. This is illustrated in figure 4.1. These solutions are usually referred to as *ghost* solutions. In this analysis, the general formalism introduced in chapter 3 is used. The rotational symmetry is taken into account by fixing the ϕ parameter. As a result, the number of free parameters in the fit is reduced to 4.

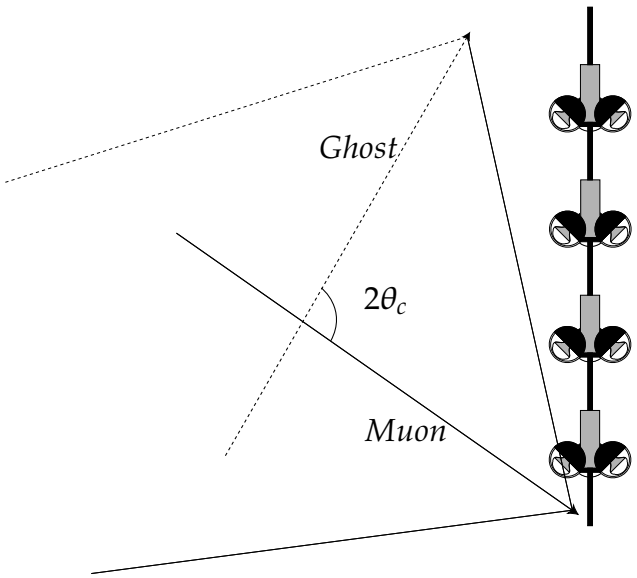

Figure 4.2: *When only one side of the Cherenkov cone of a muon is seen with a single line, an additional* ghost *solution exists. The solid lines indicate the true muon. The dashed lines indicate the* ghost *solution with its inferred missing part of the Cherenkov cone.*

4.2 Data sample

For this analysis, runs are selected from the period when Line 1 was operated stand-alone. The selected runs are flagged as 'golden' in the Antares run-selection.

A run obtains the qualification 'golden' if it meets the following requirements :

- Time lost at run start and stop is less than 100 seconds
- Total run time is more than 4000 seconds
- Trigger rate between 0.01 Hz and 10 Hz
- The baseline rate averaged over all active components should be below 120 kHz
- The burstfraction must be below 15 %

Figure 4.3 summarizes the baseline rate and burstfraction for the whole period. Each point represents the average baseline rate (figure 4.3 top) or the burstfraction (figure 4.3 bottom) for a period of 15 minutes. The black dots in the middle of figure 4.3 indicate the runs selected for this analysis. The number of runs that were selected is 63. For all selected runs, the high-amplitude threshold for L1-hits was equal to 10 photo-electrons, the standard 3D trigger was used with a minimum cluster size of 5 and event merging was on. Although the integrated running time for the selected runs is 1612764 seconds, the effective measuring time is a factor two smaller, namely 806382 seconds or about 9.3 days. This is due to the sampling factor (see section 2.6.3) which was 2 for all the selected runs. The number of triggered events written to disk during the golden runs is 75621. This corresponds to an average trigger rate of 0.094 Hz.

4.3 Monte Carlo simulation

For this analysis, a full simulation of the detector response to atmospheric muons and atmospheric neutrinos has been made. In the following a short description of the optical background, the acceptance of the optical modules and the detector geometry is given.

4.3.1 Optical background

The uncorrelated random background is simulated using the procedure explained in section 2.10. The goal is to simulate the environmental conditions, and their effects on data taking, that were present during the runs selected for this analysis. A selection is made, representing the statistical properties of the whole sample. In total 53.4 hours of data, spread over 13 runs are used. Figure 4.4 shows the distribution of rates that is used in the simulation (solid line) together with the actual measured distribution for the whole set (dashed line). By applying the trigger algorithm to data generated using this sample, the trigger rate due to uncorrelated background has been estimated. The trigger rate due to accidental coincidences was found to be less than 0.01 Hz.

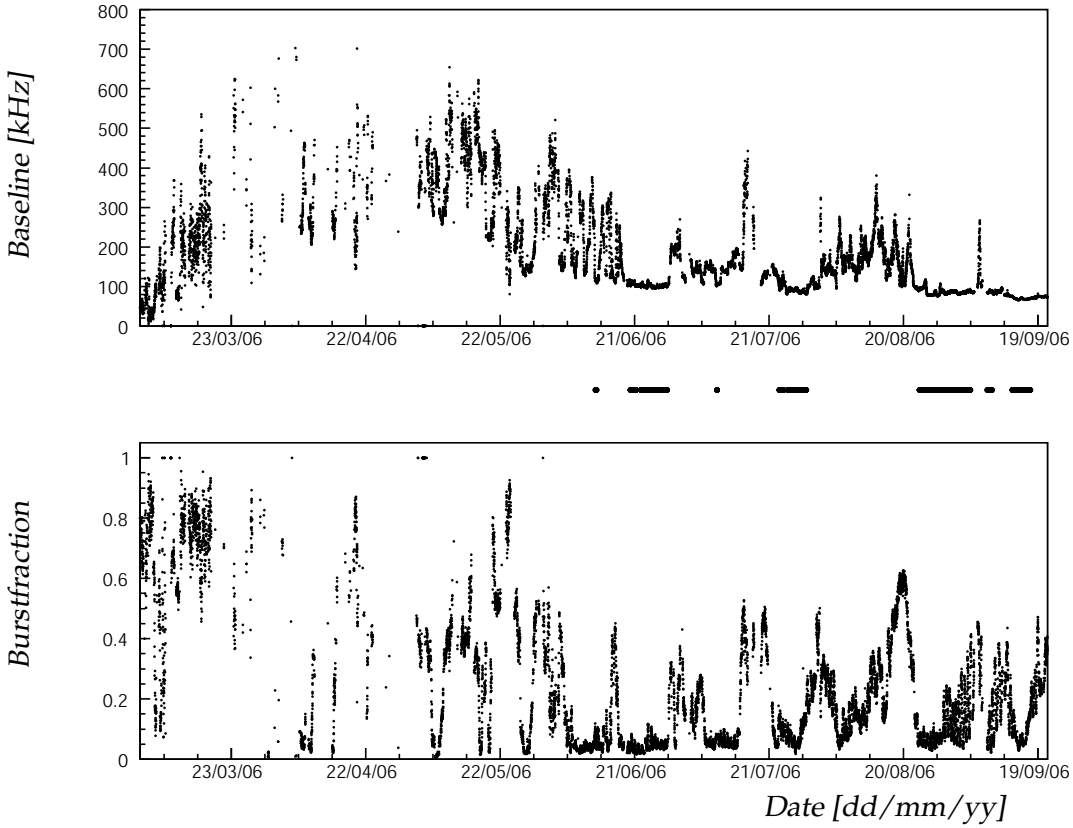

Figure 4.3: *Baseline rate (top) and burstfraction (bottom) versus time for Line 1. The black points between the plots indicate the periods selected for the analysis.*

4.3.2 Angular acceptance of the optical modules

The acceptance of the optical module depends on the angle of incidence of the photon. The optical modules are oriented downwards at and angle of 45 degrees from vertical. This maximizes the acceptance for light from upward going muons. As a consequence the photons from downward going muons hit the optical module at the edge of its acceptance, as can be seen in figure 2.5. As a consequence, a small error in the assumed acceptance translates directly to a large error in the event rate. This is taken into account as a systematic error. In order to quantify the systematic error due to the angular acceptance, an alternative parameterisation of the angular acceptance is used besides the one obtained from a measurement of the acceptance [40]. This alternative parameterisation is obtained through a ray tracing simulation of the optical module [42].

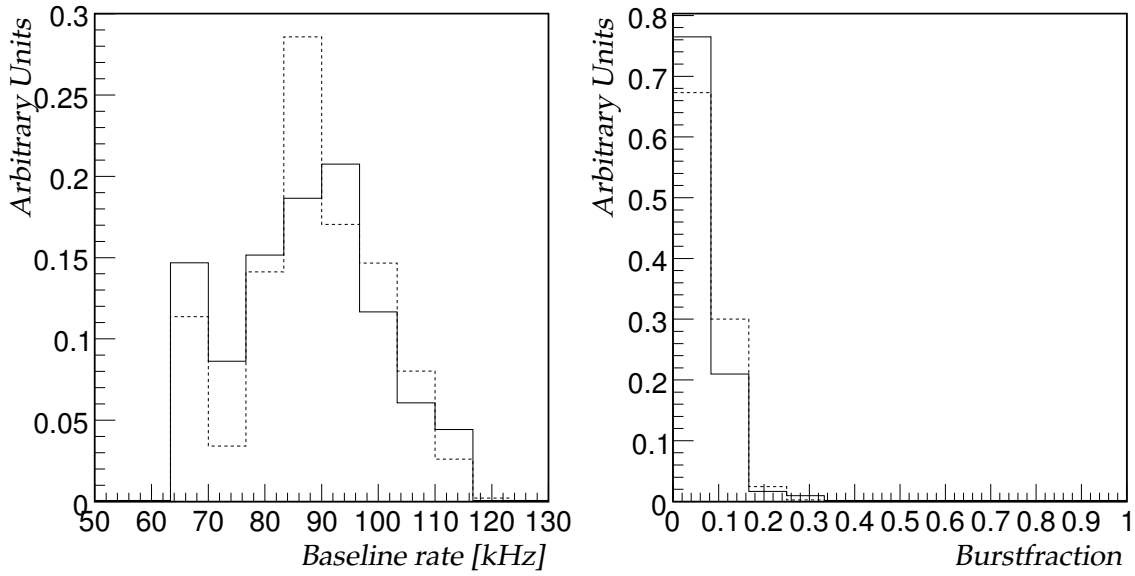

Figure 4.4: *Distribution of baseline rate (left) and burstfraction (right) for simulation (solid lines) and data (dashed lines).*

4.3.3 Line geometry

In this analysis of the data from Line 1, the detector line is assumed to be perfectly straight. Of course, in reality the line is subject to forces due to the undersea environment. Hence, the line will be bent. Two factors contribute to the uncertainty on the optical module positions. First there is the rotation of a storey around the axis. The distance from the photo-cathode of the PMT to the axis is about 56.4 cm. Ignoring the rotation of a storey introduces an error of $\sqrt{1/6} \times 56.4 \approx 23$ cm on both the x and y coordinate. The total uncertainty due to the rotation is thus about 32.5 cm. The error on the position can be transformed into an uncertainty on the timing considering the speed of light in water. The error on the timing due to the rotation is then about 1.5 ns. Second, the underwater currents can make the line sway. This makes for two effects to be considered. The current introduces relative offsets in the x-y plane between storeys. As a result, an error in the relative positioning of the storeys and thus optical modules is introduced. Figure 4.5 shows the distribution of the water-current speeds as measured with the ADCP on the MILOM for the periods of the run selection. These currents correspond to the line deviating 1 meter or less from a vertical position for 94 % of the selected data taking period. A deviation of 1 meter corresponds to an error of about 4.5 ns. The second effect of the swaying affects the absolute orientation of the line. When the detector line is tilted, while assuming a vertical orientation,

the true zenith is displaced with respect to the assumed zenith. A displacement of the top of the line of 1 meter, corresponds to a shift of the zenith of far less than 1 degree. This displacement is smaller than the expected resolution. In summary, a static alignment has been assumed in this analysis.

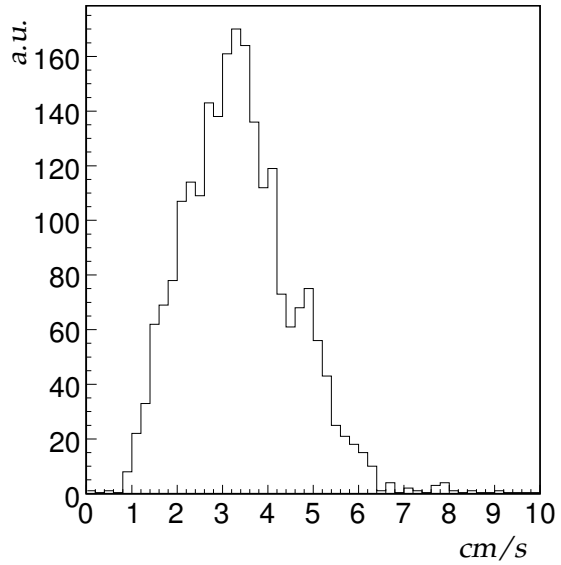

Figure 4.5: *Distribution of the water current speed as measured with the MILOM during the data taking period used in this analysis.*

4.3.4 Atmospheric muons

For this study, the atmospheric muons are generated with the fast simulation program MUPAGE, as described in section 2.10.2. For efficiency reasons, the sample was divided in two samples of different muon multiplicity (N_μ) ranges. The ranges were $1 \leq N_\mu < 30$ and $31 \leq N_\mu < 1000$. Each of the ranges represents its own equivalent livetime. In table 4.1 the atmospheric muon samples used for this study are summarized. In the table, the different (sub)samples are organised in columns. The row 'OM Angular acceptance' indicates the angular acceptance used for the samples. The row 'Multiplicity' indicates the muon multiplicity range. The row 'Generated' corresponds to the number of atmospheric muon events generated on the so-called can. The row '$N_{photons} \geq 10$' corresponds to the number of events with at least 10 detected photons. The rows 'Triggered' and 'Reconstructed' correspond to the number of triggered and reconstructed events, respectively. The row 'Livetime' corresponds to the total livetime of the sample. From this livetime, together with the number of triggered events, the trigger rate can be calculated. The trigger rate is indicated by the row 'Trigger rate'.

OM Angular acceptance	From [40]		From [42]	
Multiplicity	1-30	31-1000	1-30	31-1000
Generated	$880 \cdot 10^6$	$8 \cdot 10^6$	$440 \cdot 10^6$	$3.6 \cdot 10^6$
$N_{photons} \geq 10$	3538930	73381	2133348	35034
Triggered	70930	17184	55211	9075
Reconstructed	66925	16114	52689	8545
Livetime [day]	11.7	32.4	5.6	14.6
Trigger rate [Hz]	0.066	0.006	0.11	0.007

Table 4.1: *Sample of simulated atmospheric muons used in this study.*

4.3.5 Neutrinos

The neutrino sample consists of a mixture of muon neutrinos and anti-neutrinos. The energy ranges between 10 GeV and 10 PeV generated randomly according a $E^{-1.4}$ spectrum. Only upward going (anti-) neutrinos ($\cos(\theta) > 0$) were generated. The generation was done with the GENHEN package that is described in section 2.10.3. Table 4.2 summarizes the sample used. The sample is sub-divided in neutrinos and anti-neutrinos. The row 'Generated' corresponds to the number of neutrino interactions generated inside the so-called extended can. The other rows have the same definition as in the previous section.

Neutrino type	ν_μ	$\bar{\nu}_\mu$
Generated	$91 \cdot 10^{10}$	$110 \cdot 10^{10}$
$N_{photons} \geq 10$	330865	414859
Triggered	107279	136914
Reconstructed	106432	131256

Table 4.2: *Sample of simulated neutrino events used in this study.*

4.4 Event display

For the Line 1, the position of a hit is described by a single coordinate, namely the height z. This means that the two most important quantities for reconstruction, the position and time of the hits, can be plotted in a 2-dimensional display. Such a display is referred to as a z(t) plot. Two displays of real events are shown in figures 4.6 and 4.7. The y-axis indicates the position of the hit along the line, where $z = 0$ corresponds to the middle of the line. The x-axis gives the time at which the hit was measured, where $t = 0$ corresponds to the time of the first triggered hit. The crosses are the hits from the so-called snapshot (see section 2.8) and the black dots are hits that caused the event to be triggered. Information

about the result of the reconstruction is also shown. A square box around a hit means that this particular hit was used in the reconstruction of the event. Using the estimated track coordinates a prediction is made for the arrival time of direct Cherenkov light at a given position. This prediction is shown as the solid curve. Figure 4.6 shows an event that has hits on all the 25 floors of the line. Hits from all these floors are used to reconstruct the event. The reconstructed zenith angle of this event is about 180 degrees ; a vertically down going event. Figure 4.7 shows an event in which 8 floors are used in the reconstruction, of which 5 caused the trigger. The zenith angle of this event is about 142 degrees. In figure 4.7, the intersection of the Cherenkov cone with the detector can be recognised as the curved solid line.

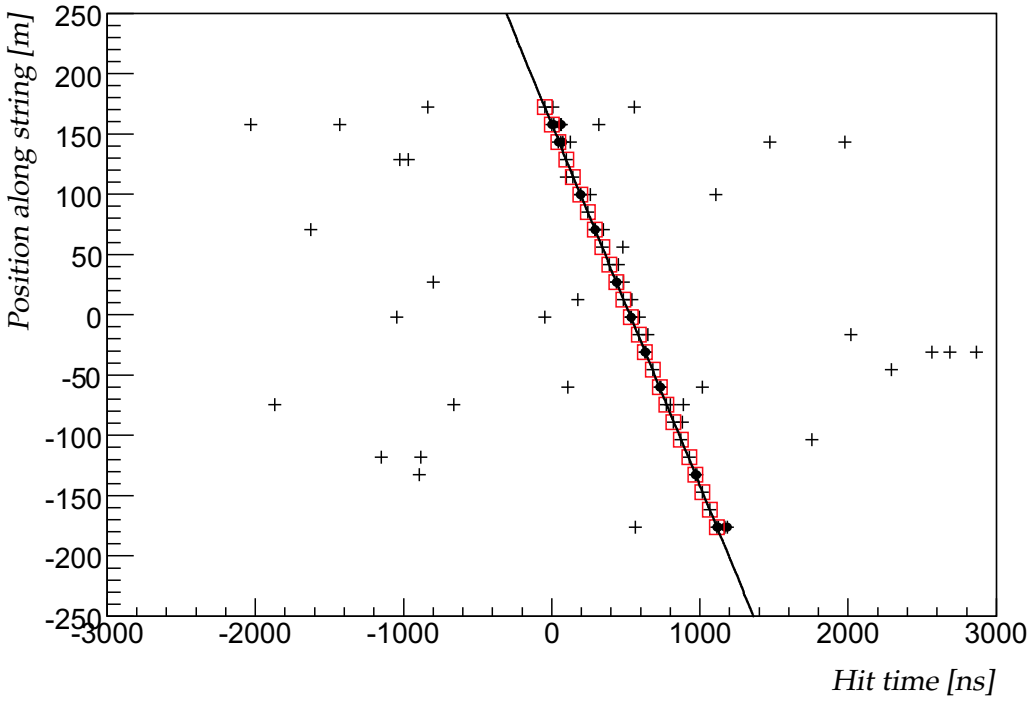

Figure 4.6: *z(t) relation for a vertically downward going reconstructed event.*

4.5 Electro-magnetic showers

Electro-magnetic showers occurring along muon tracks can show a particular signature in the detector. The first factor which contributes to this is the extension of a shower. The other factor is the angular distribution of the be emitted light. Light from an electro-magnetic shower can emitted in the complete 4π solid angle. Due

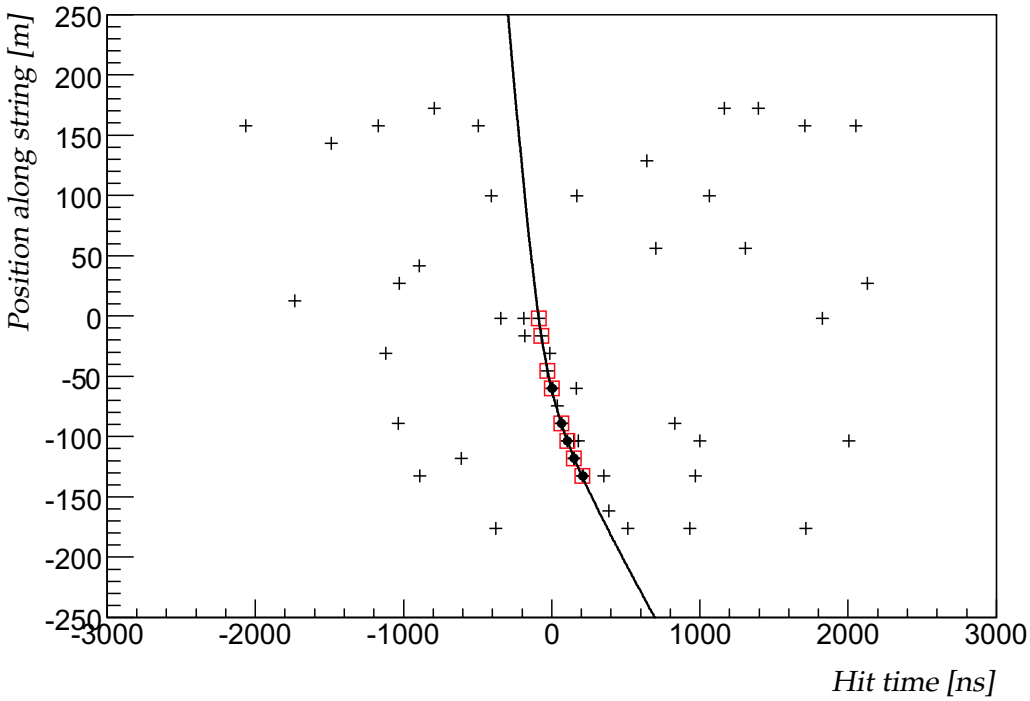

Figure 4.7: *z(t) relation for an event reconstructed with $\theta = 142$ degrees.*

to the small radiation length of water ($\sim$ 36 cm) a shower can be approximated by a point source of light. In case of a single detector line, the predicted time of a hit t_i on a optical module at position z_i along the line is given by

$$t_i = t_s + \frac{n}{c}\sqrt{d_s^2 + (z_i - z_s)^2} \tag{4.5}$$

Where t_s, z_s and d_s are the time at which the shower occurs, the height along the line and the distance from the line, respectively. The constant c is the speed of light and n the refractive index. Consider the case when $d_s^2 \ll (z_i - z_s)^2$. This occurs when the shower is close to the line or far below (above). The relation between the position and time at which the photons are detected is then linear. This linear relation between time and position is the same as the asymptotic solutions of the Cherenkov arrival time given in equation 4.4 for $\theta = \theta_c$ or $\theta = \pi - \theta_c$. Plot a) of figure 4.8 shows both the simulated z(t) relation for a muon traveling upwards with $\theta = \theta_c$ and an electro-magnetic shower occurring at 25 meters from the line. In the plots of figure 4.8, the effect of the attenuation of light with distance is ignored. Next, consider the case in which $\theta = \pi/2$ in equation 4.1, yielding

$$t_i = t_0 + \frac{\sqrt{n^2 - 1}}{c}\sqrt{d^2 + (z_i - z_0)^2} \tag{4.6}$$

This relation describes the arrival times of Cherenkov photons from a horizontal muon. It is very similar to equation 4.5. The equations differ only in the constant term in front of the square-root. Due to this similarity, a fit of a muon to a shower can result in a near-horizontal track with z_0 close to the position of the shower (z_s). The plots in figure 4.8 illustrate the z(t) relations of electro-magnetic showers and muons traveling in different directions. As can be seen from figure 4.8, electro-magnetic showers can introduce special complications when reconstructing down going muons. Photons originating from a shower and traveling in the upward direction are more likely to be detected than the direct Cherenkov photons originating from a downward going muon. This is a result of the downward orientation of the optical modules. Figures 4.9 and 4.10 show the z(t) relation of a reconstructed event. In both cases multiple solutions were found. In both figures the top plot shows the preferred solution of the reconstruction following the selection criterium introduced in chapter 3. The bottom plot shows an alternative solution with a zenith angle corresponding to a near horizontal direction. Again, the square boxes indicate the hits used for the reconstruction. The vertical solutions primarily contain Cherenkov hits from the muon while the horizontal solutions include hits from an electro-magnetic shower.

4.6 Residuals

In this section, a study of the hit time residuals will be presented. As defined in section 3.1, the hit time residual is the difference between the measured and predicted arrival time of a photon. The prediction of the arrival time is calculated assuming that the photon is emitted at the Cherenkov angle with respect to the muon direction. In the context of the reconstruction, there are two kinds of hit time residual distributions. The first kind of distribution contains all the hits that were present in the snapshot. In general, this includes background photons and late photons. The distribution of the time residuals of all hits in the event for real data is shown in figure 4.11. Several features can be distinguished. First, there is a large peak at $\Delta t = 0$ due to (direct) Cherenkov light. A second peak at about $\Delta t = 45$ ns reflects the effect of the second ARS, as explained in section 2.6.3. The tail $\Delta t \gg 0$ is due to effects such as light scattering and electro-magnetic showers. A small shoulder of negative time residuals is caused by mis-reconstructed tracks. The shoulder with positive residuals is due to the coincidence gate of the trigger, which is 20 ns. The random background can be recognised at very negative time residuals ($\Delta t \leq -100$ ns). In the second kind of distribution only the hits that are used in the reconstruction are considered. This distribution is influenced by the hit selection and hit removal procedures in the reconstruction algorithm. As explained in chapter 3 the reconstruction algorithm used in this study aims to maximize the purity of the hits with respect to the Cherenkov hypothesis. This will suppress the tail of the late photons. In the following, the

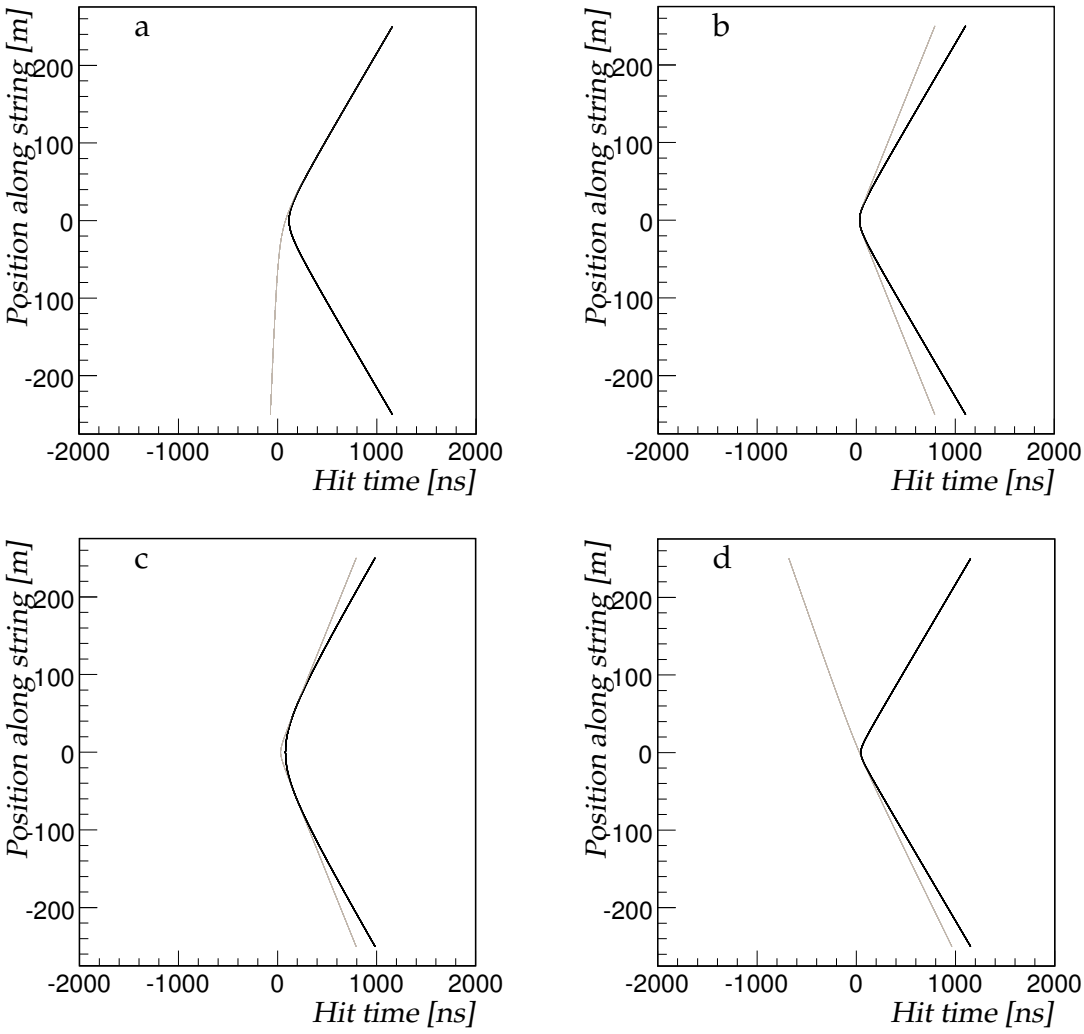

Figure 4.8: *Simulated z(t) relations for muons and electro-magnetic showers. The attenuation of the light is ignored.*
(a) A muon traveling upwards at $\theta = \theta_c$ degrees from vertical (grey line) at a distance of 25 meters for the line. An electro-magnetic shower occurs at the point of closest approach (black line).
(b) A muon traveling in horizontal direction at a distance of 10 meters from the line. An electro-magnetic shower at 15 meters from the line (black line).
(c) A muon traveling in horizontal direction at a distance of 10 meters from the line. An electro-magnetic shower at 60 meters from the line (black line).
(d) A muon traveling downwards with $\theta = 170^\circ$ at a distance of 10 meters from the line (grey line). A shower occurs at the point of closest approach (black line).

definition of a L1′-hit (see section 3.3.1) is used. With this definition of a hit, the distribution of time residuals is approximately Gaussian. When calculating the

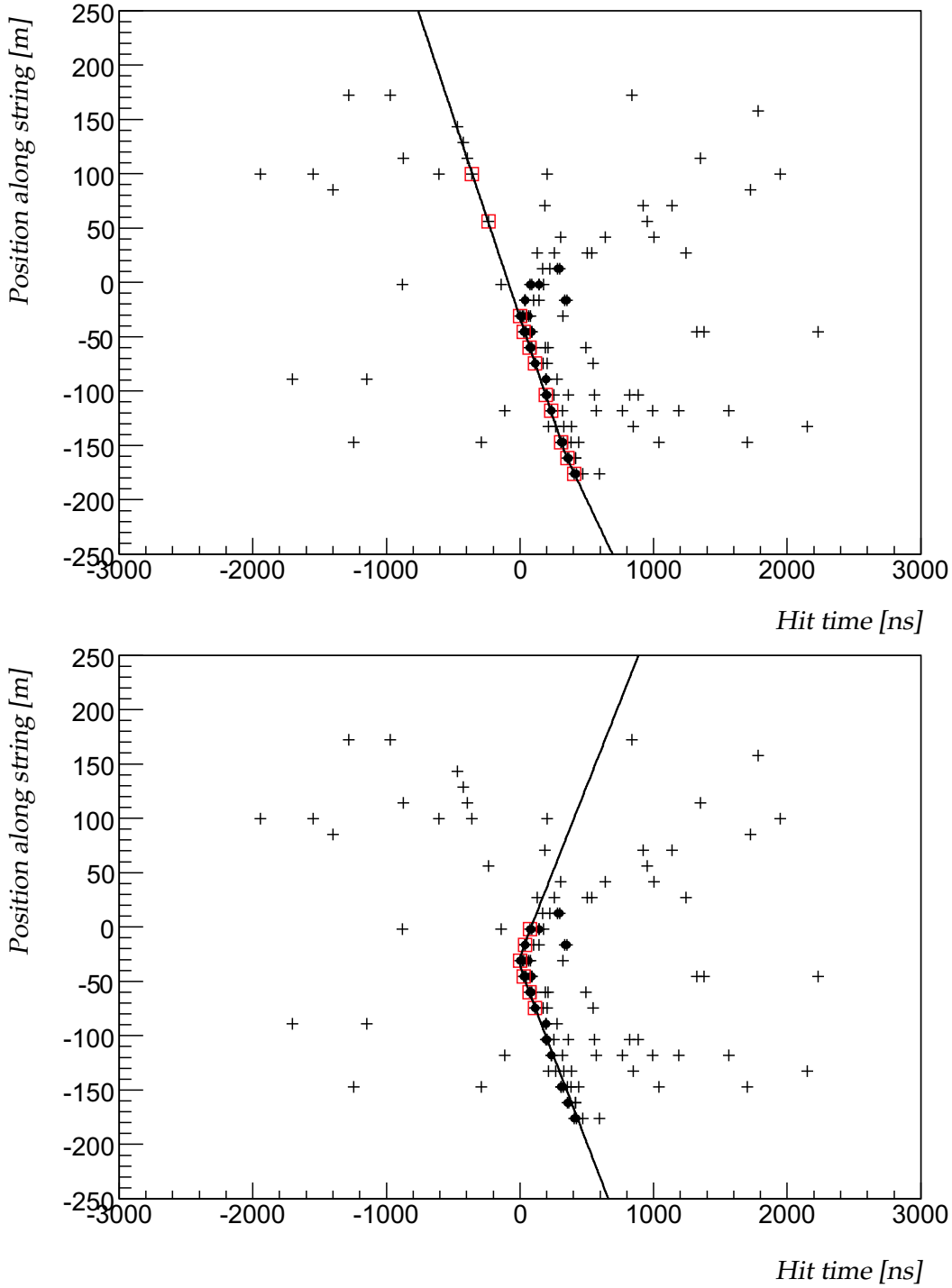

Figure 4.9: *Example of an event with multiple solutions. Top plot shows the preferred solution: a downward going muon with $\theta = 169°$. Bottom plot shows an alternative solution: a nearly horizontal going muon with $\theta = 89°$. See text.*

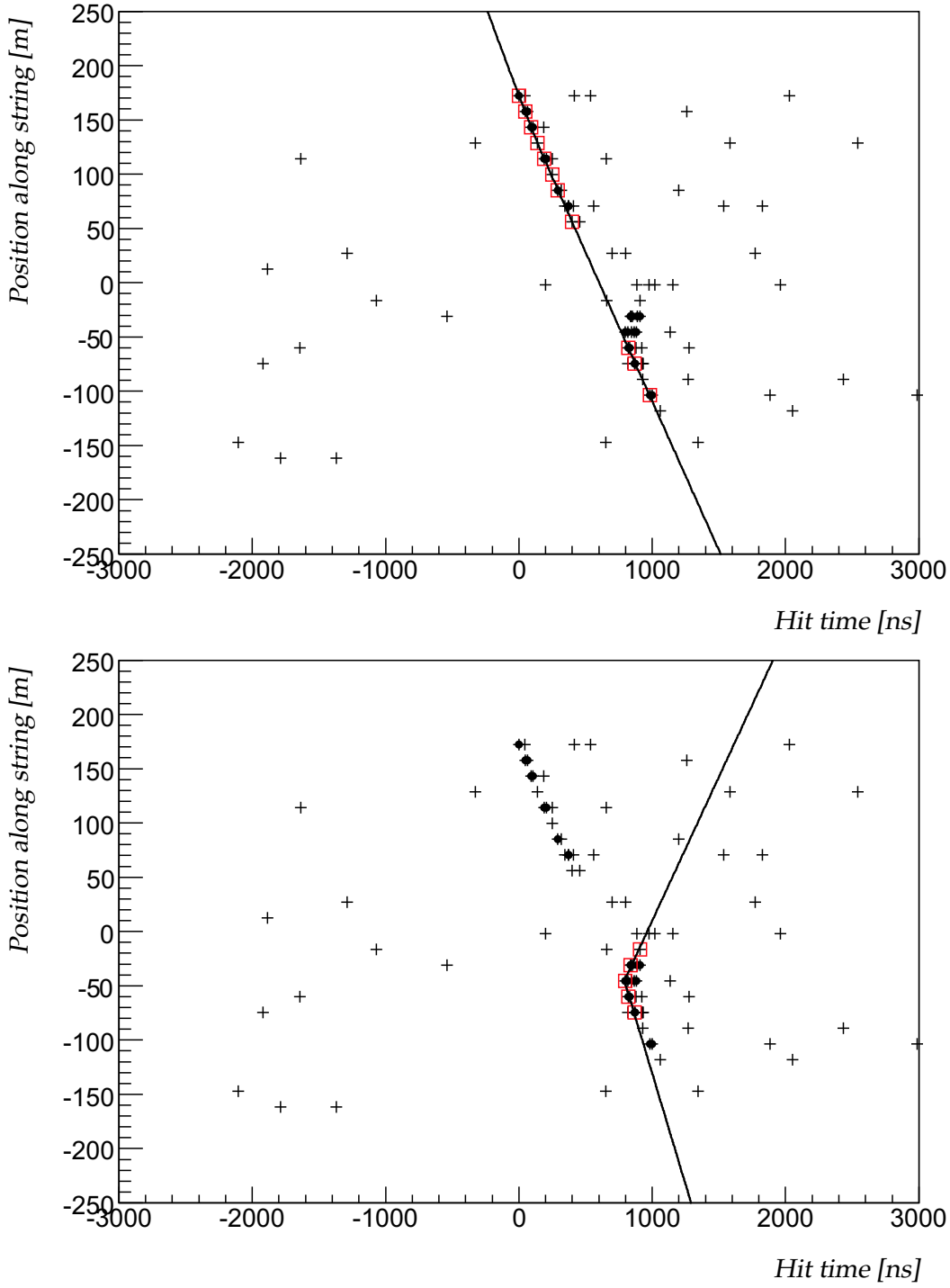

Figure 4.10: *Example of an event reconstructed with multiple solutions. Top plot shows the preferred solution: a downward going muon with* $\theta = 174°$*. Bottom plot shows an alternative solution: a nearly horizontal going muon with* $\theta = 78°$*. See text.*

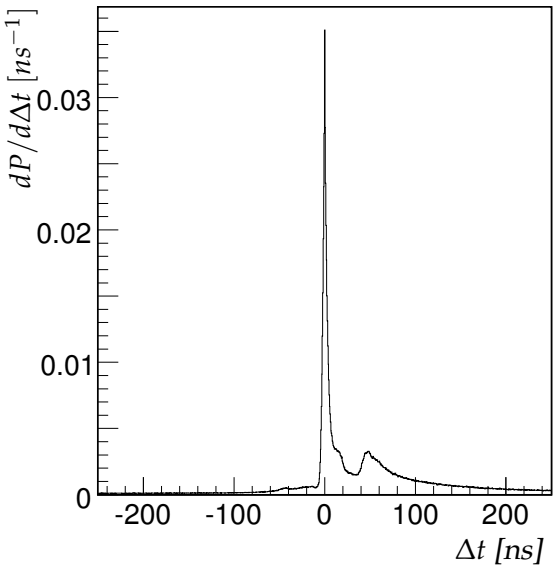

Figure 4.11: *Distribution of the time residuals for all hits in the event.*

residual, the predicted time of hit j, t_j^{th} depends on the estimated track parameters, i.e. $t_j^{th} = t_j^{th}(\vec{\theta})$. The track parameters are estimated by minimisation of the χ^2 in equation 3.4. In general, there are two scenarios to obtain the track parameters when calculating a residual.

Inclusive The hit j for which the residual is calculated is included in the minimization of the χ^2. This leads to a reduction of the dispersion of the time residuals. The underestimate becomes more prominent if the contribution of the term $(t_j - t_j^{th}(\vec{\theta}))^2$ in summation of equation 3.4 increases. This may occur when decreasing the number of hits in the sum. Of course, this pull of individual hits is also reflected in the quality of the fit, expressed as the angular residual. The dispersion on the time residuals can be small while the angular residual is large.

Exclusive The hit j for which the residual is calculated is excluded in the minimization of the χ^2. Equation 3.4 thus becomes

$$\chi^2(t_1, ..., t_n; \vec{\theta}) = \sum_{i=1, i\neq j}^{n} \frac{(t_i - t_i^{th}(\vec{\theta}))^2}{\sigma_i^2} \tag{4.7}$$

The estimated track parameters do not depend on hit j and the distribution of time residuals reflects the resolution of the hits and the accuracy of the estimated track parameters. The width of the distribution of time residuals is a result of several effects. First is the intrinsic time resolution of the measurement, indicated by σ_{int}. Second is the contribution from the error on the estimation of the track

parameters, indicated by σ_{track}. It can be calculated from the derivatives of the expected arrival times and the covariance matrix $V_{\vec{\theta}}$ of the track parameters and is given by

$$\sigma^2_{track} = \left(\frac{d\Delta t}{d\Delta\vec{\theta}}\right)^T V_{\vec{\theta}} \left(\frac{d\Delta t}{d\Delta\vec{\theta}}\right) \tag{4.8}$$

If the fit model and data agree, then these two contributions could be added quadratically, provided that the errors are Gaussian.

In figure 4.12 the inclusive and exclusive distributions of time residuals are shown. From figure 4.12 it can be seen that the exclusive distribution is broader than the inclusive, as expected. A fit of a Gaussian function in the region $-10 \leq \Delta t \leq 10$ ns gives a standard deviation of about 3.6 ns for the inclusive distribution and 5.3 ns for the exclusive distribution. As the accuracy of the fit parameters depends on the number of hits used in the fit, the same distributions are studied as function of the number of hits. Following the definition of a L1' hit (see section 3.3.1) the number of hits is equal to the number of storeys. The distributions are determined for different numbers of hits used in the fit. For inclusive residuals, this number can be as high as the maximum number of floors in the line, so 25. For exclusive residuals the maximum is 24, as the hit for which the residual is calculated is excluded. To each of the distributions a Gaussian function is fitted and the width is determined. Figure 4.13 shows the fitted widths of the distributions as function of the number of hits used in the fit. At small number of hits, several effects contribute to the width of the distributions. The dominant effect is the degradation of the fit. This effect is exacerbated by the occurrence of electro-magnetic showers and multiple muons in the event. As can be seen from figure 4.13 the inclusive residuals are affected significantly less by these effects. The different processes that contribute to the time residuals can be disentangled by a Monte Carlo simulation. Figure 4.14 shows the standard deviations of the exclusive distributions as function of numbers of hits using simulated data. The open circles include all processes and can be compared with the black circles in figure 4.13. This comparison shows a reasonable agreement between data and Monte Carlo. The squares in figure 4.14 correspond to the distributions obtained by excluding all hits caused by electro-magnetic showers in both the fit and the calculation of the time residuals. It can be seen from figure 4.14 that the distributions of the time residuals improve. This can be understood because the fit model agrees better with the selected data. The improvement is most prominent at small numbers of hits. The triangles in figure 4.14 are obtained by excluding hits from electro-magnetic showers and by selecting hits from a single track in the atmospheric shower. In this way, the fit model agrees with the selected data. Indeed, the distributions of time residuals become narrower. The only remaining effect is the possible scattering of the photons. The residual is then determined by the uncertainty of the fit (see equation 4.8).

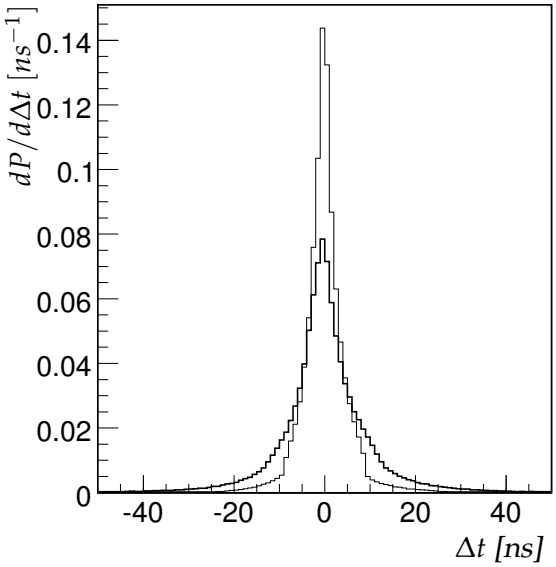

Figure 4.12: *Distribution of the time residuals obtained from real data. The black lines indicate exclusive residuals and the grey lines indicate inclusive residuals.(See text.)*

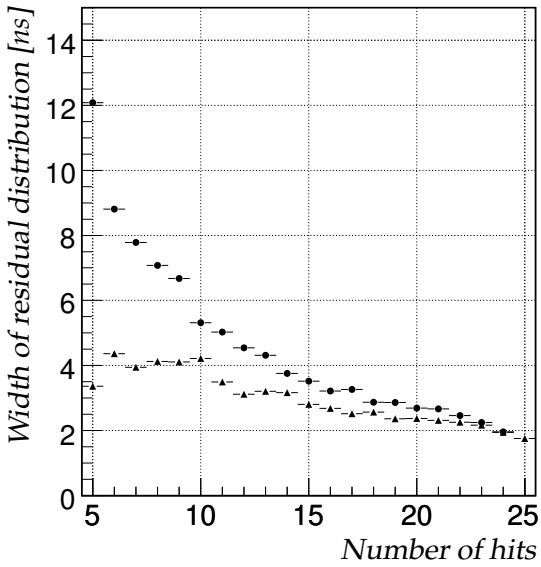

Figure 4.13: *Fitted widths of the distributions of time residuals as function of the number of hits used in the fit obtained from data. The symbols correspond to ● : exclusive residuals, ▲ : inclusive residuals.*

4.7 Zenith angle distribution

In this section the zenith angle distribution of reconstructed muons will be presented. This distribution is the result of several factors, in particular the particle flux, the detection efficiency and the reconstruction. The fluxes show a dependence on zenith angle. The muon flux originates from atmospheric showers and dominates the total flux. The detection efficiency depends on the zenith angle. The main effect is due to the geometry of the detector. Muons traveling in a near vertical direction can pass within a detectable distance from the line. Consequently, they will have a larger probability to cause hits on several floors compared to a muon traveling in a more horizontal direction. The effect of the ori-

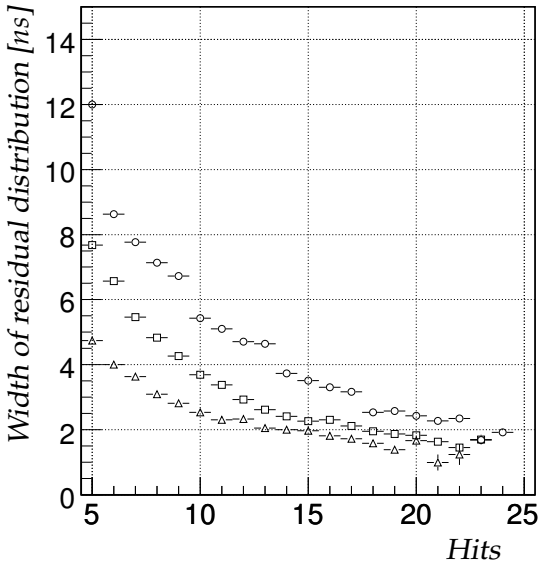

Figure 4.14: *Fitted widths of the exclusive distributions of the time residuals as function of the number of hits used in the fit obtained from simulated atmospheric muon data. The symbols correspond to ∘ : all hits, □ : only Cherenkov hits, △ : only Cherenkov hits from single tracks*

entation and the acceptance of the optical modules has been discussed in section 4.3.2. In general, the measured zenith angle of the muon differs from the actual angle. As a result of the finite angular resolution the zenith angle distribution will be smeared. Hits caused by electro-magnetic showers along the tracks, possibly complemented with other hits can cause wrong reconstruction of the track (see section 4.5). When only part of the Cherenkov cone is seen, the muon can be reconstructed at an angle $2\theta_c$ with respect to the actual muon track (see section 4.1).

4.7.1 Monte Carlo simulation

In order to estimate the effect of the angular resolution, ghost solutions and electromagnetic showers, a Monte Carlo simulation of the detector response to muons is made. The angular residual ($\Delta\theta$) is defined as the difference between the reconstructed zenith angle (θ_{fit}) and true zenith angle (θ_{true}) :

$$\Delta\theta = \theta_{true} - \theta_{fit} \tag{4.9}$$

This quantity is related to the angular residual defined in formula 3.21 by

$$\Delta a_\mu = |\Delta\theta| \tag{4.10}$$

The distribution of $\Delta\theta$ for atmospheric muons is shown in figure 4.15. In this, the events are weighted with their expected rate. The different shaded zones in the distribution indicate the contributions of events reconstructed with less than 7 hits (dark grey), 7 or 8 hits (white) and 9 or more hits (light grey). The asymmetric tail is due to mis-reconstructed events. There is a contribution of events containing hits from electro-magnetic showers and a contribution of ghost

solutions. It can be seen from figure 4.15 that the events in the tail show a small number of hits used in the fit. The median value of $|\Delta\theta|$ is about 9 degrees. As can be seen from figure 4.15 the median of the $|\Delta\theta|$ distribution decreases rapidly with increasing number of hits used in the fit. For 10 or more hits used in the fit the median is about 1.7 degrees. The dependence of the angular residual on the reconstructed zenith angle is shown in figure 4.16. The asymmetric distribution of the tail of figure 4.15 contains events that are preferably reconstructed with a zenith angle less than 120 degrees. As can be seen from figure 4.15, these events are in general reconstructed with a small number of hits.
It can be concluded that for atmospheric muons a cut on the number of hits is an effective way of improving the angular residual. It largely eliminates the tail of events that are reconstructed with a wrong zenith angle. The mis-reconstructed events could be mistakenly regarded as upward going neutrino events.
The $\Delta\theta$ distribution for upward going atmospheric neutrino events is shown in figure 4.17. The distribution is reasonably symmetric. The median of the $|\Delta\theta|$ distribution has a value of about 3.9 degrees. Requiring at least 10 hits used in the fit improves the median to about 1.1 degrees.

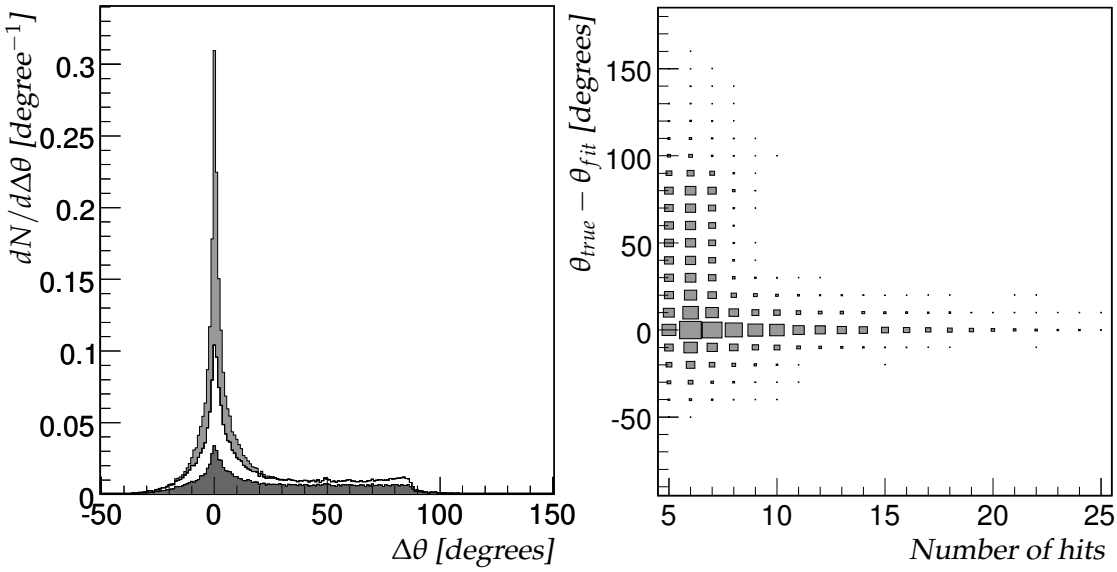

Figure 4.15: *Left: Distribution of the angular residual for atmospheric muons. Different shades indicate the numbers of hits used in the fit. Dark grey : 5-6, white : 7-8, light grey : > 8. Right: Angular residual as a function of the number of hits used in the fit.*

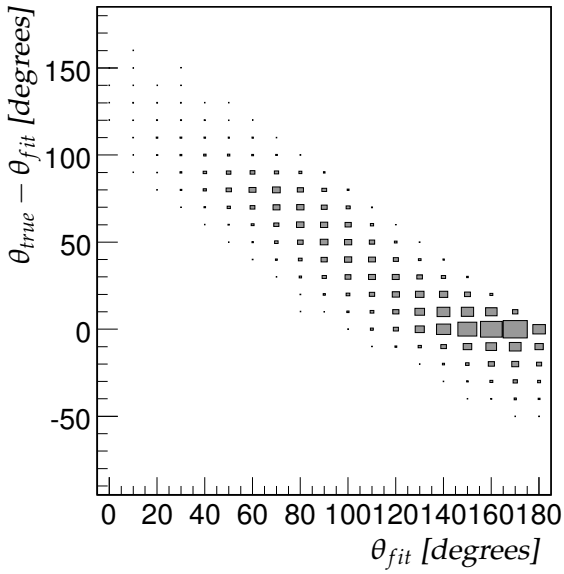

Figure 4.16: *Angular residual as function of the reconstructed zenith angle for atmospheric muons.*

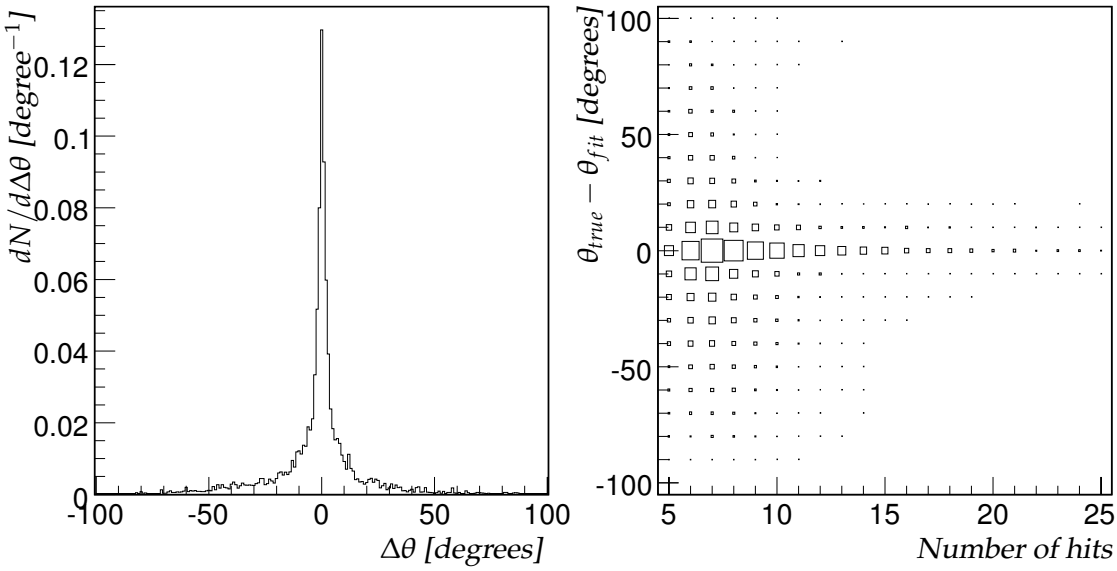

Figure 4.17: *Left: Distribution of the angular residual for atmospheric neutrino events. Right: The angular residual as function of hits used in the fit.*

4.7.2 Measured muon rate

In figure 4.18 the muon rate as function of the cosine of the zenith angle is shown. In the figure, both the measured and the simulated data sets are shown. The simulated data set consists of the atmospheric muons presented in section 4.3.4. The same selection is applied to both the data and the Monte Carlo data. The

requirement for an event to be included is that at least 5 hits, and thus 5 storeys, were used to reconstruct the event. The measured data points only have statistical errors drawn. The band drawn for the simulated data contains the systematic error due to the angular acceptance of the optical modules and the statistical error. The distributions of data and Monte Carlo simulation agree reasonably well. The

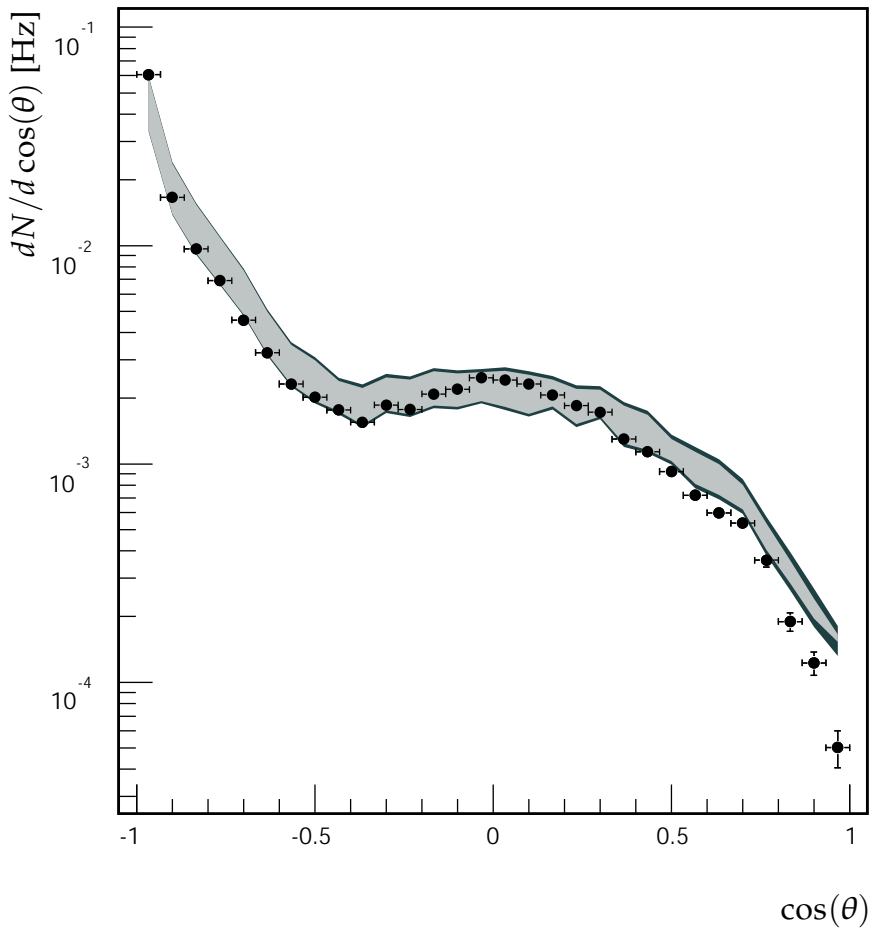

Figure 4.18: *Measured muon rate as function of the cosine of the reconstructed zenith angle. The points correspond to the data. The band corresponds to the Monte Carlo simulation. The width of the band indicates the systematic error (light grey) and the statistical error (dark grey).*

distribution is strongly peaked at $\cos(\theta) = -1$ which corresponds to the vertical downward direction. This confirms the general picture that the muon flux is dominated by atmospheric muons. The bump occurring between $\cos(\theta) = -0.5$ and $\cos(\theta) = 0.5$ reflects the tail in the $\Delta\theta$ distribution from figure 4.15.

4.7.3 Angular resolution from data

The Antares detector is built up of identical detection units, the storeys. Any set of the storeys can be regarded as a detector. This means that the detector can be split in parts to perform consistency checks and cross-calibrations. This section describes an estimation of the angular resolution. In order to facilitate the estimation of the resolution, the detector line can be split in two parts with nearly identical properties. These two parts are denoted by A and B, each consisting of a set of storeys. Zenith angles reconstructed with set A (B) are referred to as θ_A (θ_B). In order to estimate the angular residual from the real data, the difference between the reconstructed zenith-angles using sets A and B is studied :

$$\Delta\theta_{A-B} = \theta_A - \theta_B \tag{4.11}$$

The uncertainty of θ_A and θ_B are assumed to be equal and are denoted by $\Delta\theta_{A/B}$. Assuming a Gaussian distribution of $\Delta\theta_{A/B}$, the standard deviations of $\Delta\theta_{A/B}$ and $\Delta\theta_{A-B}$ are related by

$$\sigma_{\Delta\theta_{A/B}} = \sigma_{\Delta\theta_{A-B}}/\sqrt{2} \tag{4.12}$$

For a Gaussian distribution, the median of the absolute deviation is related to the standard deviation by a numerical factor, thus

$$median(|\Delta\theta_{A/B}|) = median(|\Delta\theta_{A-B}|)/\sqrt{2} \tag{4.13}$$

For this study, Line 1 was split up in two different ways. For the first split, the odd floor numbers belong to set A, the even floor numbers to set B. This way of splitting is referred to as the *even/odd* split. The other split divides the line in a top and bottom part. The top 13 floors belong to set A, the remaining 12 floors belong to set B. This way of splitting is referred to as the *top/bottom* split. The number of events reconstructed with each of the subsets are summarized in table 4.3. The third row in the table gives the number of events that were reconstructed for both subsets. The numbers in this row correspond to the events that can be used to estimate the angular resolution. Thus for the *even/odd* split, 4007 events are reconstructed in both subsets and for the *top/bottom* 2211 events. The yield of reconstructed events differs significantly between the *even* and *odd* sets and between the *top* and *bottom* sets. This is linked to the numbers of working optical modules in each of the subsets. In total there were six optical modules which have no recorded data in the selected data sample. Only one out of these six was on an *odd* floor, and four out of the six were located in the *top* half of the detector.

The measured distributions of $\Delta\theta_{A-B}$ are shown in figure 4.19. The median of the $|\Delta\theta_{A-B}|$ distribution of the *top/bottom* sets is about 11.8 degrees, while for the *even/odd* sets it is about 3.7 degrees. This gives a median angular residual for the

even	8001	top	29075
odd	12172	bottom	37142
even & odd	4007	top & bottom	2211

Table 4.3: *Numbers of reconstructed events for different sub-divisions of the Line 1.*

top or bottom set of about 8.4 degrees and for the even or odd set of about 2.6 degrees. It should be noted that the *even/odd* sets span a larger length of the detector line. A larger length of the track reduces both the probability of a ghost solution and the influence of electro-magnetic showers along the track. The *top/bottom* sets correspond to different parts of the track. Hence, an electro-magnetic shower affects usually one of the sets. This can result in a large difference between the reconstructed zenith angles. The effect of the χ^2 probability and the number of hits used in the fit is also studied. In figure 4.20, the median of the $|\Delta\theta_{A-B}|$ distribution is shown as function of the minimum number of hits used in the fit (with and without a cut on the χ^2 probability). The requirement of the minimum number of hits is on *both* fits. For the cut on the χ^2 probability of larger than one percent, a resolution 1.75 ns is assumed. The medians of $|\Delta\theta_{A-B}|$ decrease when more hits are required for the fit. This decrease is consistent with figure 4.15. For the *top/bottom* split the angular residual drops below 3 degrees when at least 10 hits are required. For the *even/odd* split, the angular residual drops below 1 degree. According to formula 4.13 this leads to a median angular residual of about 2.1 degrees for the *top/bottom* split and about 0.7 degrees for the *even/odd*. This implies that the resolution of the complete line, thus when combining the even and odd parts, can reach about 0.5 degrees.

4.8 Vertical muon intensity

The reconstructed number of events as function of $\cos(\theta)$ is shown in figure 4.18. The number of detected events in a $\cos(\theta)$ bin i depends on the muon flux $\mathcal{F}_i$ in that bin and the detector acceptance. The detector acceptance includes the detection efficiency and the effects from the reconstruction. The detector acceptance can be described by a two-dimensional matrix R_{ij}, as events can migrate to a different bin due to the finite angular resolution. With $\mathcal{N}$ bins covering $\cos(\theta) \in [-1, 1]$, the measured rate F_i is related to the flux by

$$F_i = \sum_{j=0}^{\mathcal{N}} R_{ij}\mathcal{F}_j \tag{4.14}$$

When the angular resolution is small compared to the bin size the off-diagonal elements of R_{ij} will be close to zero, i.e. $R_{ij} = 0$ for $i \neq j$. In this case the matrix

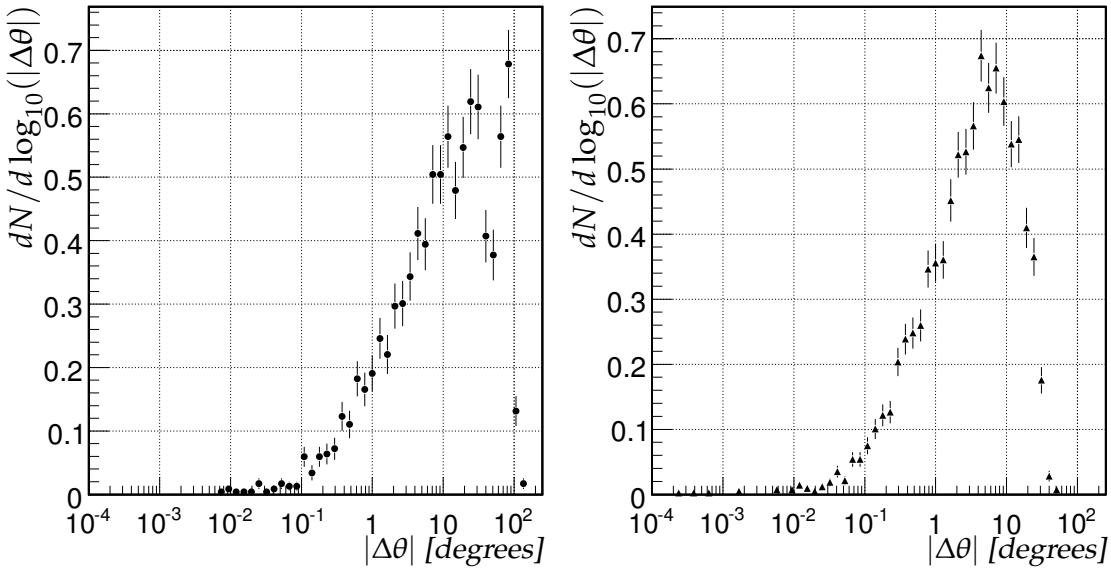

Figure 4.19: *Distributions of the angular residual $|\Delta\theta_{A-B}|$ between the results of the reconstruction with the line split up in a top and bottom part (left) or an even and odd part (right).*

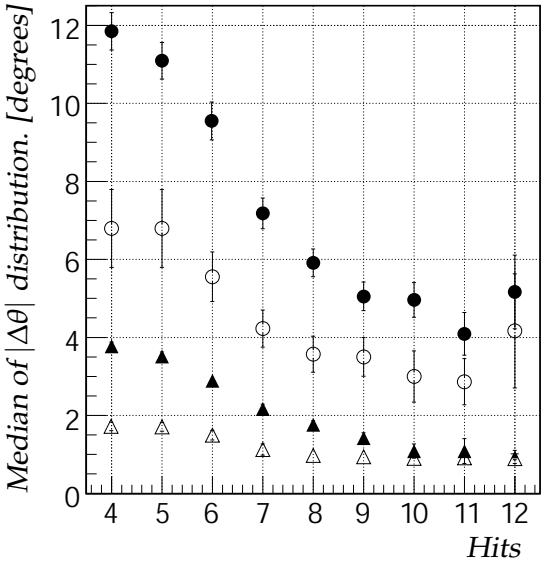

Figure 4.20: *Medians of the distributions of the angular residual ($|\Delta\theta_{A-B}|$) between the different reconstructions with the line split up in a top and bottom part (circles) or an even and odd part (triangles). Plotted as function of the minimum number of hits used in both lines. The open symbols have a cut on χ^2 probability of greater than one percent applied.*

R_{ij} becomes a 1 dimensional vector R_i and equation 4.14 reduces to

$$F_i = R_i \mathcal{F}_i \tag{4.15}$$

The flux can be determined if R_i is known by

$$\mathcal{F}_i = \frac{F_i}{R_i} \tag{4.16}$$

The values of R_i can be estimated from a simulation of the detector response to muons. From the simulation, the muon flux $\mathcal{F}_i^{sim}$ and the simulated rate F_i^{sim} are then known. The detector response R_i^{sim} can then be determined by the ratio of F_i^{sim} and $\mathcal{F}_i^{sim}$:

$$R_i^{sim} = \frac{F_i^{sim}}{\mathcal{F}_i^{sim}} \tag{4.17}$$

It should be noted here that R_i^{sim} is not an unbiased quantity and in general differs from the true detector response R_i. The reason for this is that it is derived from a simulation, which includes an assumed flux. Hence, R_i^{sim} can be considered as the detector acceptance for an *assumed flux*. This correction includes muons which are below detection threshold.

For this work, the muon flux is obtained with the parametric simulation MUPAGE, described in section 2.10.2. In figure 4.21 the values of R_i^{sim} for the different $\cos\theta$ bins are shown. The cross-bars on the errors indicate the systematic error due to the angular acceptance of the optical modules. With increasing $\cos(\theta)$, the values of R_i^{sim} change gradually with a maximum deviation between two consecutive bins of about a factor two. For values of $\cos(\theta)$ in excess of -0.5 the correction factor increases rapidly because of an overestimation of the true detected rate due to bin migration. The bins with $\cos(\theta) > -0.5$ are increasingly contaminated with wrongly reconstructed events due to showers and ghost solutions. For the estimation of the vertical muon flux the bins with $\cos(\theta) > -0.5$ are excluded. By replacing R_i by R_i^{sim} in equation 4.16, the muon flux for the different $\cos(\theta)$ bins can be determined. The result is shown in figure 4.22. Each value of the zenith angle corresponds to a certain slant depth through the water mass above the detector. The measured muon flux can also be given as a function of slant depth. In order to calculate the muon vertical intensity, the distribution of muons at sea level has to be taken into account. This distribution (see reference [79]) is given by

$$\frac{dN_\mu}{dE_\mu} \approx \frac{0.14 E_\mu^{-2.7}}{cm^2\ s\ sr\ GeV} \left(\frac{1}{1 + \frac{1.1 E_\mu \cos(\theta)}{115 GeV}} + \frac{1}{1 + \frac{1.1 E_\mu \cos(\theta)}{850 GeV}} \right) \tag{4.18}$$

For a given value of $\cos(\theta)$ formula 4.18 is integrated over the energy range from 2 TeV to 10 PeV and the relative values are used to correct the vertical muon intensity. The resulting depth-intensity relation of the vertical muon intensity is shown in figure 4.23. The results obtained in this analysis agree well with those obtained in other experiments.

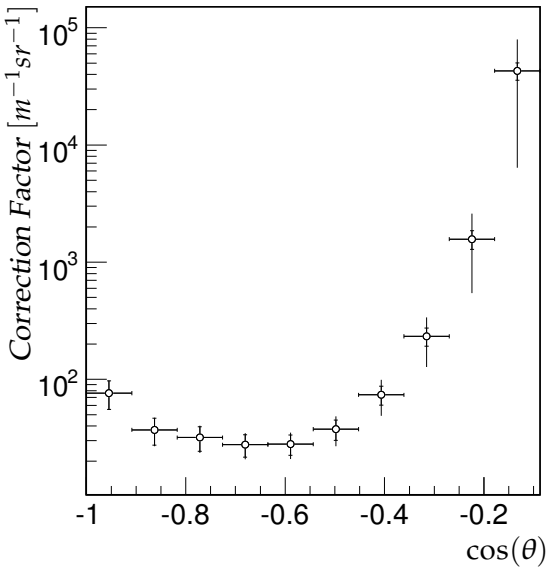

Figure 4.21: *Correction factor R_i^{sim} as function of the cosine of the reconstructed zenith angle. The vertical cross-bars indicate systematic errors. The horizontal cross-bars indicate the bin size.*

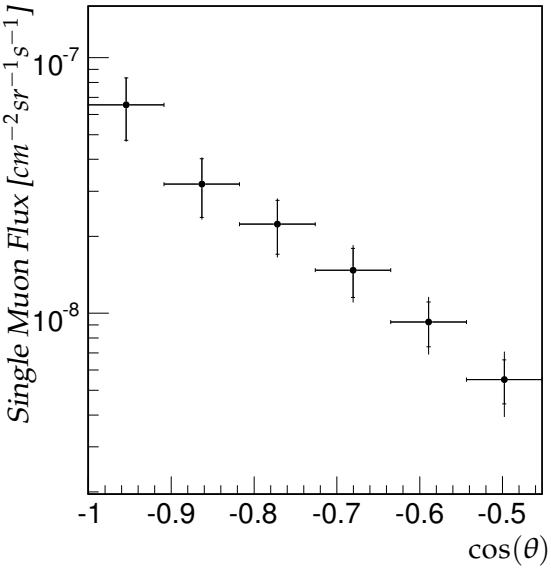

Figure 4.22: *Single muon flux as function of $\cos(\theta)$ corrected for the detector acceptance. The vertical cross-bars indicate the systematic errors. The horizontal cross-bars indicate the bin size.*

4.9 Neutrino candidates

From the simulation, it is expected that the reconstructed event sample should contain a small number (≈ 4) of upward atmospheric neutrino-induced events. However, there are 9515 upward reconstructed events. These events are dominated by mis-reconstructed atmospheric muon events (see section 4.7). There are two main quantities which give a handle on the angular resolution of the reconstructed events and the purity of the upward reconstructed events, namely the number of hits used in the reconstruction and the χ^2 probability of the final fit. From the data and simulation, events have been selected which are reconstructed as upward going and have a χ^2 probability greater than one percent. In figure 4.24

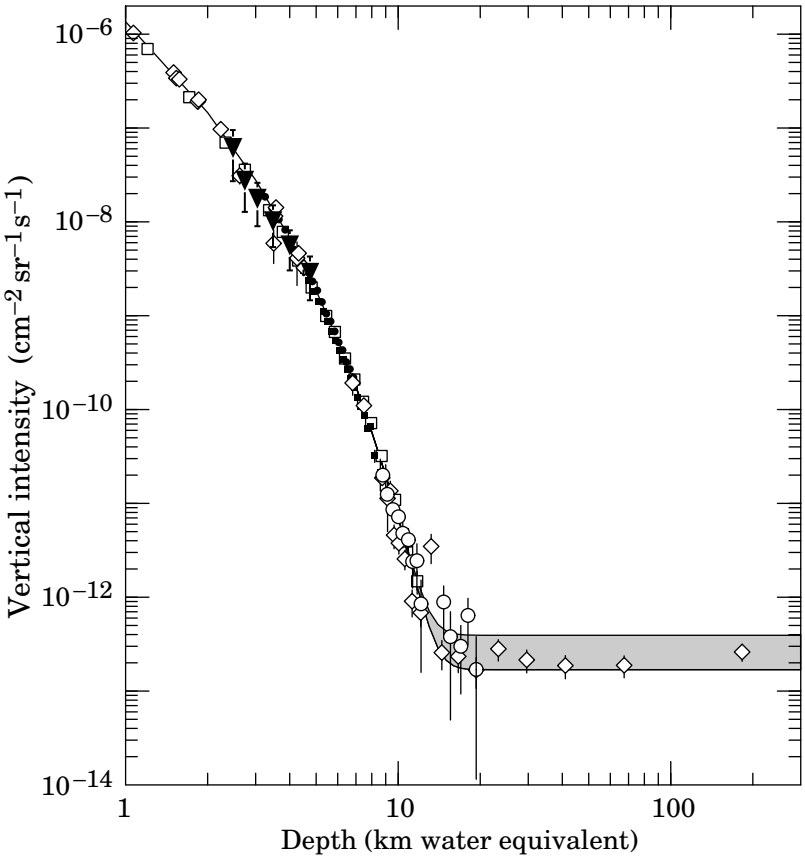

Figure 4.23: Vertical muon intensity versus depth. ▼ : This work. Plot taken from [14].

the number of remaining events is shown as a function of the minimal number of hits used in the final fit. The data agree reasonably well with the simulation of atmospheric muons. The simulation indicates that there are no atmospheric muons to be expected with more than 9 hits used in the reconstruction. The data contain one event that is reconstructed with 10 hits. This event is consistent with the predicted atmospheric neutrino flux. Figure 4.25 shows the display of this event. The hits used in the fit are found above and below the point of closest approach to the line, which are both L0 and L1 hits. There is no apparent signature of an electro-magnetic shower, confirming that this event can be considered as a neutrino induced muon.

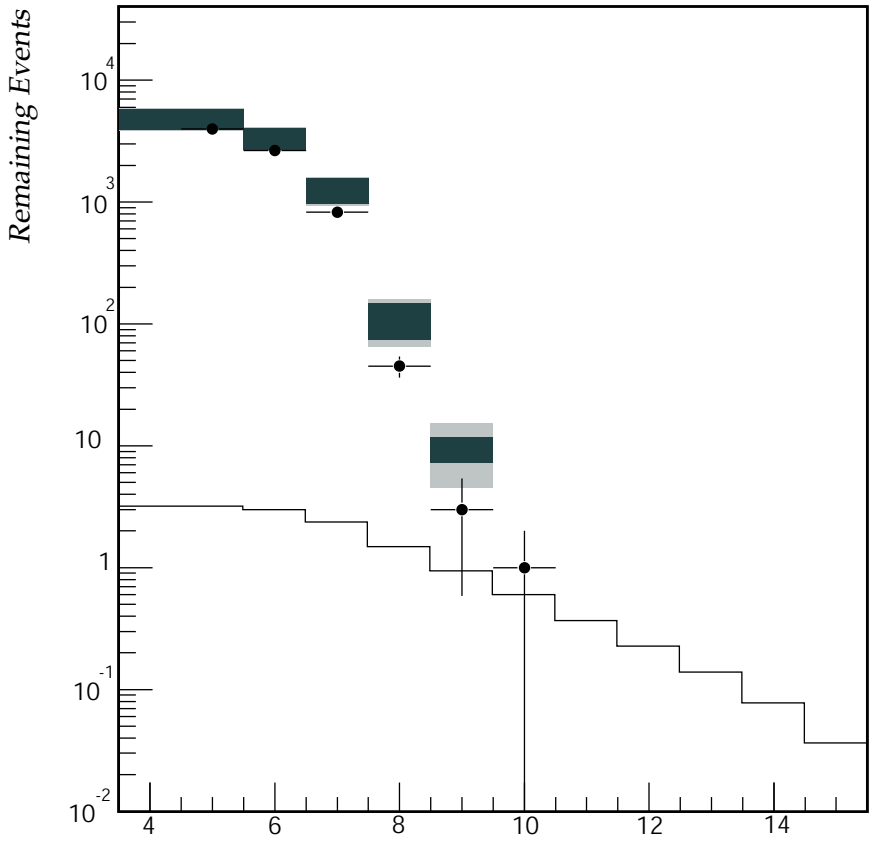

Figure 4.24: *Remaining number of events reconstructed as upward going as function of the minimum number of hits used in the fit. The points correspond to the data, the grey bands to the contribution from wrongly reconstructed atmospheric muons and the histogram to the contribution from genuine upward going atmospheric neutrino events. The height of the dark grey bands indicates the systematic error, the light grey bands correspond to the total error.*

4.10 Conclusions

An analysis was performed on the data of the first detector line of the Antares neutrino telescope. Monte-Carlo simulations were done to enable a confrontation with data and to evaluate the performance of the detector and track reconstruction. As the main signal consists of atmospheric muon tracks, the analysis was mainly focused on these events. After determining the detector response, the vertical muon intensity as function of depth in water could be constructed. The measured vertical muon intensity is consistent with other experiments (see for example [14]). Also, a search for neutrino candidates was done, resulting in

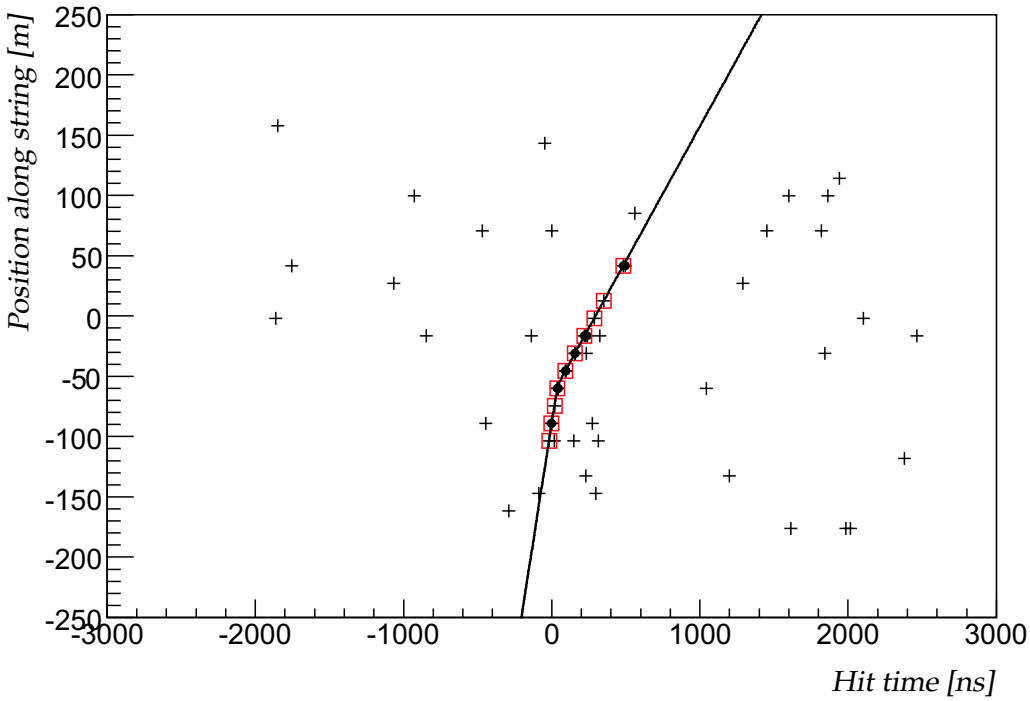

Figure 4.25: *Neutrino candidate event. The reconstructed zenith angle is* $\theta = 30^\circ$.

one candidate.

The occurrence of electro-magnetic showers along muon tracks is the leading contribution to the error in the determination of the zenith angles of muon tracks. This is emphasized for atmospheric muons due to the orientation of the optical modules. A bias to more horizontal zenith angles is introduced when hits from electro-magnetic showers are included in the hit selection. This effect contributes to atmospheric muon events being falsely identified as upward going events. The resemblance of electro-magnetic shower dominated events to horizontal tracks leads also to an underestimation of the χ^2 error. The fraction of electro-magnetic shower events can be significantly reduced by requiring a minimum number of hits used in the fit due to the local nature of these events. The distribution of the residuals of hit times and its dependence on the number of hits used in the fit agree well between simulation and data. The contributions of electro-magnetic showers and muon bundles to the distributions of the hit time residuals were identified in simulation. These contributions were found to be significant at lower numbers of hits used in the track fit. While the simulation of photon arrival times seems to be in good shape, there is an uncertainty in the angular acceptance of the optical modules. This uncertainty introduces a systematic error in the estimation of event rates and detector acceptance. The measured rates are largely within

these errors.

The angular resolution of the detector line was studied by making use of the atmospheric muon data, without relying on simulation. A resolution of better than 1 degree for the zenith angle can be achieved without even utilizing the whole line. The estimate of the resolution of the complete detector ($< 0.3^\circ$, see chapters 3 and 5) seems realistic. Also because of the good agreement between the simulated measured distributions of the hit time residuals.